Mathematical Biosciences 383 (2025) 109430

Contents lists available at ScienceDirect

Mathematical Biosciences

journal homepage: www.elsevier.com/locate/mbs

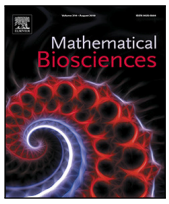

Original research article

Analyzing time activity curves from spatio-temporal tracer data to determine tracer transport velocity in plants

Hannah Lanzrath [a,c,d], Eric von Lieres [b,c,d], Ralf Metzner [a,d], Gregor Huber [a,d,*]

[a] Forschungszentrum Jülich, IBG-2: Plant Sciences, 52428 Jülich, Germany
[b] Forschungszentrum Jülich, IBG-1: Biotechnology, 52428 Jülich, Germany
[c] RWTH Aachen University, Computational Systems Biotechnology, 52074 Aachen, Germany
[d] Forschungszentrum Jülich, Center for Advanced Simulation and Analytics (CASA), 52428 Jülich, Germany

ARTICLE INFO

Keywords:
Plant
Tracer
Transport
Velocity
Time activity curve
Model
Positron emission tomography

ABSTRACT

Non-invasive methods utilizing tracers have a great potential to investigate carbon allocation in plants. Specifically, radioactive tracers, such as ^{11}C, enable the monitoring of spatially localized transport processes on short time scales in living plants. Typically, such tracer transport experiments yield time activity curves (TACs) of tracer activity over time at various locations along a transport pathway. These TACs can exhibit different characteristic shapes that strongly depend on tracer transport dynamics, reflecting properties such as transport velocity, exchange with surrounding tissue, and tracer storage along the pathway. Various methods, either data-driven or model-based, exist to determine transport velocities from TACs. However, for some TAC shapes, the inferred carbon tracer velocity values can be inconsistent and greatly vary between analysis methods. In the present study, we review and evaluate different analysis methods for their suitability to reliably determine tracer transport velocities from typical TAC shapes. For this evaluation, we use both *in silico* generated and experimentally acquired TACs from positron emission tomography measurements on tomato, barley, and bean. We demonstrate that each of the compared methods can be suitable for specific TAC shapes while being less or not appropriate for others. In conclusion, we present a case-specific evaluation of methods as a reference for analyzing TACs from tracer transport experiments, which allows to ensure a robust and globally comparable determination of transport velocities.

1. Introduction

Despite a century of research in the field of long-distance transport in higher plants, the underlying mechanisms of carbon allocation still remain unclear [1–4]. The delicate structure of the phloem poses an ongoing challenge for undisrupted, real-time analysis of assimilate transport. Non-invasive methods such as tracer studies that utilize the short-lived radioisotope ^{11}C do not interfere with the carbon transport while enabling analysis in intact plants and have been established over the last decades [5–10]. In such experiments, the tracer is typically fed to the plant as $^{11}CO_2$ over a short time span. The allocation of the assimilated carbon isotope through the plant's vascular tissue can be traced with positron emission tomography (PET), providing spatio-temporal 3D information about the movement of the tracer pulse over the duration of the experiment. Unlike ^{13}C, ^{14}C and other tracers, the approach combining ^{11}C and PET provides high-resolution spatio-temporal tracer data, enabling accurate and in-depth analysis of transport dynamics. Time-activity curves (TACs) derived from such 3D data show tracer activity at defined locations along the transport pathway. The shapes of these TACs reflect the underlying transport dynamics, depending on transport velocity, exchange with surrounding tissues, and tracer storage along the pathway [11]. Deriving transport velocities from these TACs is of special interest for functional phenotyping of plant traits under varying environmental conditions [6,12]. Various approaches to analyze tracer transport velocity have been published: Data-driven methods exploit curve characteristics, for example, by comparing the times of tracer pulse arrival at the detector site or the times at half height of the curve [13–17]. These methods typically disregard mechanistic and physiological considerations. In contrast, model-based approaches aim to explain the origin of the curve shape [18]. Mechanistic model approaches [7,19] additionally encode multiple other transport properties alongside transport velocity.

In this study, we evaluate and compare different readily available analysis methods for determining tracer transport velocities from TACs.

* Corresponding author at: Forschungszentrum Jülich, IBG-2: Plant Sciences, 52428 Jülich, Germany.
E-mail address: g.huber@fz-juelich.de (G. Huber).

https://doi.org/10.1016/j.mbs.2025.109430
Received 30 August 2024; Received in revised form 10 December 2024; Accepted 11 March 2025
Available online 19 March 2025

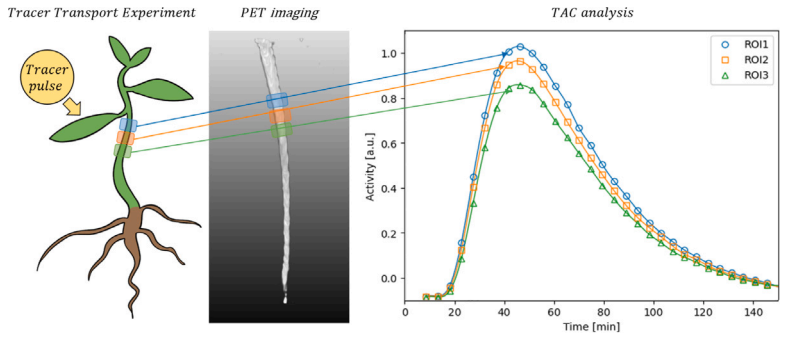

Fig. 1. Schematic of time-activity curve acquisition: The three regions of interest (ROIs) in blue, orange and green in the PET image correspond to three distinct spatial locations of the plant. The ROIs are manually placed to analyze the 3D PET data with MeVisLab. The tracer accumulated inside each ROI results in a time-activity curve (TAC) that can be further analyzed. The data shown is not decay-corrected and scaled to a maximum of 1.

To conduct this evaluation, we utilize both *in silico* generated and experimentally acquired TACs, the latter obtained from PET measurements on three plant species: tomato, barley, and bean. The goal is to provide a case-specific assessment of the suitability of various methods, serving as a reference for robust and globally comparable determination of transport velocities in tracer transport experiments.

2. Methods

2.1. Data acquisition

For each tracer transport experiment, a single plant leaf was sealed into a cuvette and pulse-labeled for 6 min with a gas mixture containing the radioactive tracer $^{11}CO_2$ at atmospheric concentration. The $^{11}CO_2$ tracer was produced through the $^{14}N(p,\alpha)^{11}C$ nuclear reaction by irradiating nitrogen in a gas target with 18 MeV protons. Details of the trapping device used to collect $^{11}CO_2$, as well as the gas exchange and labeling system, are provided in Metzner et al. [20]. The PET measurement system 'PhenoPET' used in the experiment is a custom-built vertical-bore instrument specifically designed for plant measurements [21]. Further details about the plants' growth conditions and the protocol of tracer transport experiments with the PhenoPET are specified in Appendix A.

The three-dimensional spatio-temporal PET image data were processed and visualized in MeVisLab 3.4. (MeVis Medical Solutions AG, Bremen, Germany) as described in Metzner et al. [20]. Supported by a custom-written MeVisLab tool [22], virtual cylindrical detectors were placed to define specific regions of interest (ROI) along the transport axis. These detectors have set dimensions which determine their length and diameter. Tracer activity inside each ROI is integrated over defined time intervals resulting in a TAC (Fig. 1).

2.2. The impact of decay correction on data error

The shape of TACs acquired as described in Section 2.1 is dominated by the radioactive decay of the short-lived radioisotopes used as tracers. For the data to accurately represent transport dynamics, this influence of radioactive decay needs to be taken into account, i.e., the curves must be decay-corrected. From the experimentally observed data $D(t)$, the initial tracer concentration D_0 can be reconstructed, assuming $D(t) = D_0 \cdot \exp(-\lambda t)$, where λ is the decay constant. Increasing uncertainties in later data points due to decay correction are here visualized in simulated data by adding a realistic noise of 0.7% (see Section 2.3.5) to the raw data (Fig. 2). It is important to note that the exponential effects of the decay correction on the uncertainty of the data are often neither discussed nor considered, although they can strongly influence the data analysis.

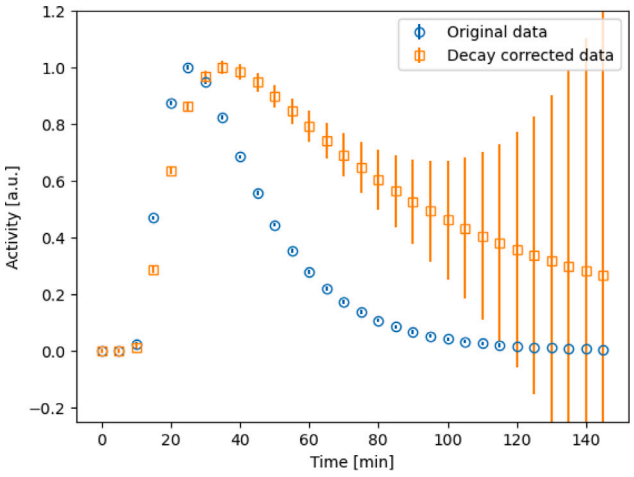

Fig. 2. The effect of decay correction on the uncertainty of data as simulated with a realistic error margin of 0.7% following Bühler et al. [23]. Both TACs are scaled to a maximum of 1.

2.3. Methods for velocity estimation

The tracer transport velocity is typically calculated from the mean distance ^{11}C tracer travels over a specific period. As the location x_i and, consequently, the distance Δx_i between the centroid of either virtual or real detectors i are usually predetermined, most methods used to determine tracer transport velocity aim to identify a *reference time* t_i corresponding to a specific feature in the TAC (and thus in the pulse within the detector's field of view). The tracer flow velocity, v, can then be estimated as the slope of a linear fit, $x_i = v \cdot t_i + x_{t=0}$, to the distance-time observations. The relative standard deviation can be calculated from the variances found in the diagonal of the corresponding covariance matrix.

In the following, four methods, three of which determine reference times based on TAC shapes and one mechanistic approach directly estimating a model velocity, are introduced and their strengths and weaknesses are evaluated.

2.3.1. Time of first arrival - intercept method

The time when the tracer pulse first arrives at the detector field of view is a characteristic point of a TAC. The velocity calculated from the times of first arrival constitutes a front velocity of the pulse and can be considered as the maximum velocity. A time of arrival could be determined by the time when the signal surpasses an arbitrary threshold (Fig. 3a, green dashed line). However, this approach is highly sensitive to noise in the tracer activity signal. Hence, the time of pulse arrival is more frequently estimated making use of the intercept

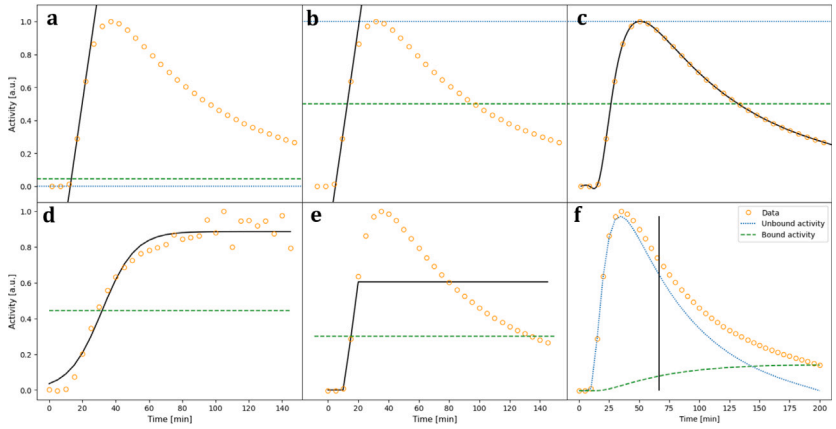

Fig. 3. Demonstration of the data driven analysis methods introduced in Section 2.3 on simulated tracer transport data (see Section 2.3.5). Showcased are the Intercept method (a), the Half-maximum method with linear regression (b), a spline (c) or logistic regression (d)–(e) and the McKay model (f). The orange circles are the datapoints. Simulated data in panels (a)–(c) and (e)–(f) resemble typical experimental data without noise in the form of a pulse activity over time. In panel (d) an example of a high storage with noise was chosen to showcase the application of logistic regression. In panels (a)–(e) the black line is the regression curve. In panel (a) the blue dotted line equals the zero line, the green dashed line marks an threshold value that has to be surpassed to mark the time of arrival. In panels (b)–(e) the green dashed line equals the half-maximum. In panels (b) and (c) the blue dotted line marks the maximum. In panels (a)–(e) t_i is given by the intersection of the green dotted line and the black regression line. In panel (f) the blue dotted line marks the unbound activity, the green dotted line marks the bound activity and the black vertical line equals t_i.

method [13,17]. The intercept method identifies a linear part in the pulse increase (Fig. 3a, black line) and calculates the time of first pulse arrival as the point where the regression line crosses zero tracer activity. In the cited works, identification of the linear part of the curve relied solely on visual inspection of the TACs. There have been attempts to minimize the subjectiveness and variability in this approach by choosing the slope through binning candidates of arrival times in a histogram [16]. However, this introduces additional parameters that must be chosen individually and can influence the determined time of arrival. As part of our study, we propose an alternative by utilizing the RANSAC algorithm (Section 3.1.2) to minimize discrepancies between determined velocity and true velocity that can otherwise be caused by subjective choices and manual errors.

2.3.2. Time at half-maximum - half-maximum method

Comparing times at which signals reach half-height of their maximum is a known approach throughout different fields and has also been utilized in tracer transport analysis [15,17]. In this method, the maximum of the curve is determined, halved, and the first time at which half-maximum is reached is considered as reference time point for each ROI. Analyzing half-maximum times focuses on the steepest segment of the TACs slope. This avoids a common issue encountered when directly comparing peak maxima, i.e., flat or noisy peaks resulting in increased variability in the x values (time) between closely spaced y coordinates (activity). Hence, using the half-maximum reduces the influence of measurement errors and complete failures of the method caused by peak maxima that are difficult or impossible to identify.

Compared to the intercept method this approach estimates an average time of arrival instead of the time of first arrival. As the highest point of the TAC does not necessarily represent the true peak maximum, especially for noisy data or data with low resolution, the position of the true maximum needs to be reconstructed. Also, the point at the half-maximum has to be determined through interpolation of the data. This can be done by fitting a linear regression curve through the TAC slope (Fig. 3b) or polynomial regression to the whole TAC. Alternatively, we here propose an approach employing splines (Fig. 3c) to approximate the TAC shape, as it allows for the simultaneous identification of the peak maximum and half-maximum as well as their corresponding times. For unclear maxima which resemble a noisy point cloud without a decline, either calculating the average height of the points in the cloud or logistic regression (Fig. 3d) may be applicable to estimate the maximum. The logistic regression assumes a sigmoidal (s-shaped) curve, categorizing points between a minimum and maximum. The inflection point equals the point at the half-maximum and can be directly derived from the regression formula. Note that logistic regression cannot be applied to TACs with peaking pulse shapes (Fig. 3e).

2.3.3. Compartmental model according to McKay

McKay et al. [18] introduced a kinetic tracer model that assumes unidirectional tracer movement along a transport pathway, where at position x_i tracer can get irreversibly stored with probability s_i [1/mm] per spatial unit. The measured pulse signal $M_i(t)$ [Bq/mm] is modeled as the sum

$$M_i(t) = G_i(t) + B_i(t) \tag{1}$$

of the mobile radiotracer $G_i(t)$ and immobilized radiotracer $B_i(t)$. The mobile tracer is assumed to have a bell shape, resulting in $G_i(t = \infty) = 0$ and therefore, according to Eq. (1), $M_i(t = \infty) = B_i(t = \infty)$, presupposing that the measured signal at the last time point equals the signal at $t = \infty$ and therefore is equivalent to the immobilized tracer. At each position, i, tracer is immobilized at a rate of

$$dB_i(t)/dt = s_i v_i G_i(t) = s_i v_i (M_i(t) - B_i(t)). \tag{2}$$

The immobilized tracer $B_i(t)$ per unit length at any given time t can then be calculated as the integral from 0 to t:

$$B_i(t) = s_i v_i \int_{\tau=0}^{\tau=t} (M_i(\tau) - B_i(\tau)) d\tau \tag{3}$$

and the mean arrival time at position i is given by

$$t_i = \frac{\int_{t=0}^{\infty} t G_i(t) dt}{\int_{t=0}^{\infty} G_i(t) dt}. \tag{4}$$

This derivation is explained in detail in McKay et al. [18].

Converse et al. [24] applied this method to analyze PET tracer data by determining the mean arrival time t_i at given ROI i and calculated tracer transport velocity v_i using the known distance between the ROIs center points. An example of the separation of the TAC into mobile and immobilized tracer is shown in Fig. 3f.

2.3.4. Compartmental models according to Bühler et al.

Bühler et al. [7] introduced a family of compartmental models, rooted in the works of Horwitz et al. [25] and Tyree et al. [11]. These models incorporate plant mechanistic properties while selectively considering only a subset of physiological parameters, avoiding issues of

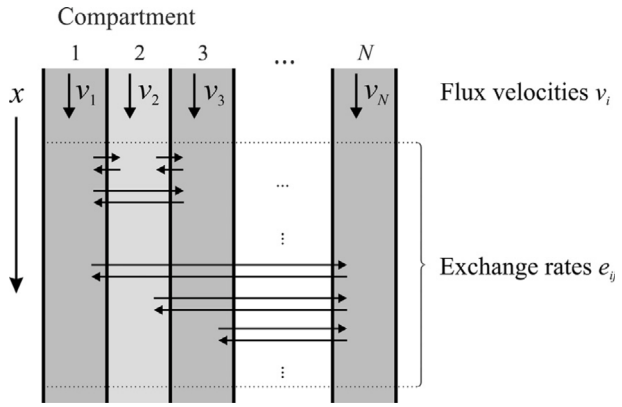

Fig. 4. Architecture of multichannel transport model class with N one-dimensional spatially parallel compartments, flux velocities v_i and exchange rates e_{ij} between compartments i and j.
Source: Figure taken from Bühler et al. [7].

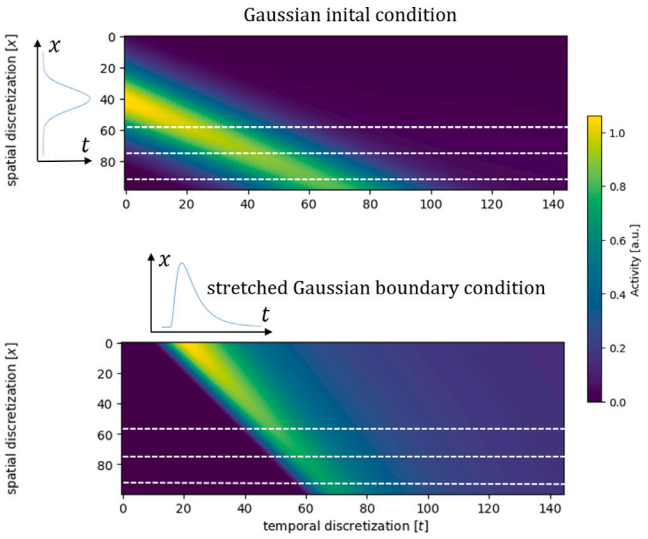

Fig. 5. Spatio-temporal tracer distribution of two simulated datasets (see Section 2.3.5). The upper one with a Gaussian initial condition and the lower one with a stretched Gaussian boundary condition. The dotted white lines mark the ROIs.

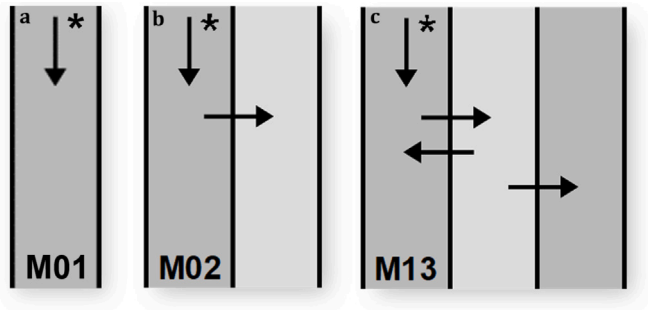

Fig. 6. A subset of the multichannel transport model class (see Fig. 4): M01 (a) with only one flux velocity, M02 (b) with a flux velocity and a storage parameter, M13 (c) with a flux velocity, storage, and exchange parameters.
Source: Figures taken from Bühler et al. [7].

excessive complexity and parameter abundance seen in physiological models. Notably, this approach differs from the previously introduced methods by simultaneously fitting TACs of every ROI instead of determining reference times for each TAC. Furthermore, radioactive decay is explicitly included into the model equations, enabling direct analysis of non-decay-corrected original data and thereby avoiding data errors introduced by decay correction (Section 2.2). The primary concept of this model family is to enable mechanistic modeling of spatio-temporal tracer transport while maintaining simplicity without anatomical specifics and requiring minimal fit parameters [26]. Under the name multichannel transport (MCT) model, the model family was now added as an extension of the CADET solver, a software package originally developed in the field of chromatography modeling [27], which is freely accessible under the GPL license (https://cadet.github.io). All simulations in this study were performed using the MCT model integration and the reaction module of CADET [28], included in the currently published development version and will be part of a full release in the future [29].

The general model class (Fig. 4) comprises N one-dimensional spatially parallel compartments, within each of which axial tracer transport can occur at flux velocities v_i. In addition, tracer can be laterally exchanged between any two compartments, denoted as i and j, with a rate constant e_{ij}. This results in a coupled system of partial differential equations (PDEs)

$$\frac{\partial \boldsymbol{\rho}(x,t)}{\partial t} = \left(A^T - V\frac{\partial}{\partial x} + D\frac{\partial^2}{\partial x^2} \right) \boldsymbol{\rho}(x,t), \tag{5}$$

where $\boldsymbol{\rho} = (\rho_1 \dots \rho_N)^T$ describes the tracer density within each compartment N at position x and time t. The coupling matrix A contains exchange rates e_{ij} describing the lateral tracer transport from compartment i to compartment j. The decay of a radioactive tracer is included at a tracer-specific rate λ. The diagonal matrix V contains the flux velocities v_i and the diagonal matrix D contains the dispersion coefficients d_i for each compartment. For a more thorough exploration of the mechanistic assumptions underlying each term and the numerical solution approximation of the PDEs, additional details can be found in Bühler et al. [7,30] and the CADET documentation.

Solving these equations yields the spatio-temporal distribution of tracer activity (Fig. 5). From this, TACs can be determined for each ROI, corresponding to the locations of the virtual detectors marked by the dotted white line in Fig. 5. The model parameters can be estimated by fitting these simulated TACs to the corresponding observed TACs. The fit quality can be assessed using the mean squared error (MSE), which quantifies the deviation between the fit and experimental data.

In Bühler et al. [7,23,26,30] the compartmental models have been used assuming a local initial condition represented by a Gaussian curve (Fig. 5 upper). This means tracer activity enters the system as a spatial distribution at time $t = 0$. In the present work an asymmetric boundary condition at $x = 0$ was used instead (Fig. 5 lower). This 'stretched Gaussian' is similar to a log-normal distribution and defined as

$$y = p_1 \exp\left(-\frac{1}{2}\left(\ln((t-p_3)/(p_2-p_3))/\ln p_4\right)^2\right). \tag{6}$$

This asymmetric boundary condition has the advantage of more accurately describing tracer profiles observed after CO_2 uptake through plant leaves compared to the symmetric Gaussian curve as initial condition.

Although the family contains numerous models, with their specific architectures listed in detail in Bühler et al. [7], a smaller subset often proves adequate for describing TACs across most plant species. Model M13 (Fig. 6c) includes phloem unloading/reloading as well as storage and can sufficiently describe most cases in which these processes are significantly contributing. Conversely, in cases where such exchange is absent and the tracer is just transported while being stored along the transport axis or redirected into lateral branches, Model M02 (Fig. 6b) often provides a suitable fit. Model M01 can describe dynamics when neither storage nor exchange processes are present and the TAC is characterized solely by the transport (Fig. 6a).

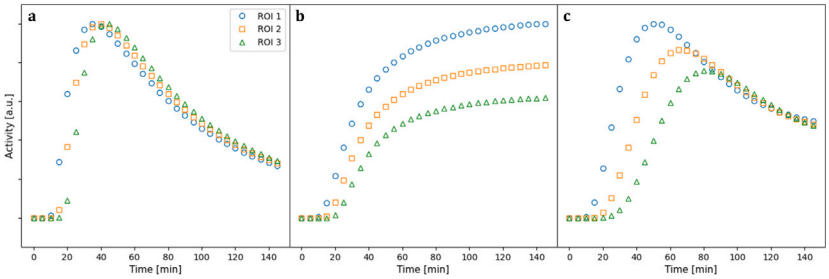

Fig. 7. Examples of three transport types that are commonly observed in tracer transport experiments. Data was simulated with model M01 (a), model M02 (b) and model M13 (c). TACs at different ROIs of Uniform transport (a) and Storage type transport (b) have the same shape, only shifted in height due to loss or storage or in time due to the velocity. The curve shape changes for Exchange type (c) transport, due to the unloading and reloading of the tracer.

2.3.5. Creation of artificial reference data with the Bühler model family for three different transport types

In the present study, several reference data sets were created to enable a controlled investigation of analysis methods. These data sets reflect *in vivo* transport dynamics observed in tracer transport experiments and match those in the case study to ensure comparability. Here, we distinguish three types of transport dynamics. For simplicity, these are referred to in the following as 'Uniform', 'Storage', and 'Exchange'. To facilitate visual observation of transport dynamics, all of the depicted TACs are decay-corrected (Fig. 7). The Uniform transport type (Fig. 7a) is dominated by the tracer moving as a closed faction with very little or no exchange and storage effects. The shape of the TAC at the different ROIs therefore either does not change or only changes in height in between curves due to little loss or storage along the transport axis. When observing this transport type, a clear maximum of the pulse is visible in the decay-corrected curves. The Storage type describes transport that involves substantial storage along the transport axis (Fig. 7b), resulting in curves with a plateau instead of a maximum peak. The Exchange type is dominated by unloading and reloading processes surrounding the phloem in addition to transport and storage (Fig. 7c). This results in a change of shape between the curves acquired at different ROIs. Transport types can differ between different plant organs of the same plant or between plant species *in vivo*.

The reference data for any of the three transport types were generated using the Bühler model family. For each transport type, the best-fitting model from the model family was selected based on its ability to describe the experimental data while adhering to rational criteria to avoid overfitting, as detailed in Bühler et al. [7]. There, the Uniform transport type relates to either model M01 or model M02 with no or only little storage. The storage-dominated transport was modeled with model M02 with a high storage rate. With exchange parameters allowing to model tracer transfer between multiple compartments, model M13 was used to simulate the Exchange transport type with changing curve shapes. Fig. 6 illustrates the hierarchical structure of these models, where an increasing number of parameters corresponds to progressively more complex transport dynamics.

For every reference data set at $x_0 = 0$ the stretched Gaussian distribution was used as a boundary condition. The parameters used to create the respective artificial data for each experiment, table, or figure are specified in Appendix B.1. The choice of model parameters was based on typical fit parameters for the respective curve shapes, that correspond to the intended transport dynamics. To simulate a model error that matches the noise on real data, normally distributed noise with a standard deviation of $7e{-}3$ was added to the simulated data. This is analogous to Bühler et al. [23] and matches a typical error analyzing TACs from sugar beets [7].

3. Results and discussion

3.1. Evaluation of methods

3.1.1. Effect of data noise on methods

Tracer transport data acquired by PET measurements is naturally subject to a range of possible errors, caused for example by the way of detection and correction or weak signals resulting in noisy data. This noise is exponentially amplified by the necessary decay correction of the raw data (see Section 2.2), especially noticeable towards later times (see Fig. 8, right column). To test the noise sensitivity of the introduced methods, we analyzed the ability to retrieve a known tracer transport velocity of two simulated datasets: one without noise and another with added Gaussian noise of 0.7% (see Section 2.3.5). Both datasets match the Uniform transport type, characterized by the absence of storage and exchange processes, with a defined maximum peak.

Except for the McKay model, each of the introduced methods performed well for the noiseless data (Results in Table 1 and Fig. 8, left column).

In case of the noisy data set (Fig. 8, right column), similar differences in method performance were observed. The Intercept and Half-Maximum methods make use of early parts of the TAC that are not much affected by the exponentially growing noise. Therefore they perform similarly for noiseless and noisy data, with velocity estimations close to the true velocity of 5 mm/min (Table 1). The Bühler model performed well for both, noiseless and noisy data, also indicated by very small MSEs of $1.71e{-}07$ for the noiseless and $6.22e{-}5$ for the noisy case. The model compensates for uncertainties through noise by fitting all TACs at the same time instead of analyzing each one separately. The relative difference of 0% in the noiseless data case is expected, as the data was created with a model of the Bühler model family.

The high relative standard deviation (7.4%) of the Intercept method and the failure of the McKay method are investigated further in the next two sections.

3.1.2. Effect of choice of the linear part of curve on the intercept method

As the intercept method determines the reference times t_i by extrapolating from the linear part of TACs, the analysis is sensitive to the distance between the linear part and the time-axis, as well as to the choice of which points to include when assuming that linear part. In the literature, the determination of the linear part of the curve has often been performed by the mere judgment of the user. To avoid the subjectivity of manually identifying the linear slope, in this study the intercept method was combined with the RANSAC algorithm [31]. The RANSAC algorithm identifies points in a dataset that fit a linear relationship, allowing for a specified error margin. The algorithm requires a minimum of four data points as potential candidates for the linear region of the curve to operate effectively.

To investigate how variations in the slope affect velocity estimation, a simulated dataset was created using model M01 and a velocity of $v = 5$ mm/min, to serve as a ground truth. Then a 'standard RANSAC' analysis was performed with the intercept method utilizing the RANSAC

Table 1
Derived velocities from simulated data (see Section 2.3.5) with Intercept method, Half-maximum method, McKay model and Bühler model. Reference velocity 5 mm/min.

		Method			
		Intercept	Half-maximum	McKay model	Bühler model
Noiseless	v [mm/min]	4.97 ± 7.4%	5.02 ± 0.4%	6.72 ± 0.2%	5.00 ± 0.0%
Noisy	v [mm/min]	5.01 ± 7.8%	4.90 ± 1.8%	−0.05 ± 1919%	5.02 ± 1.5%

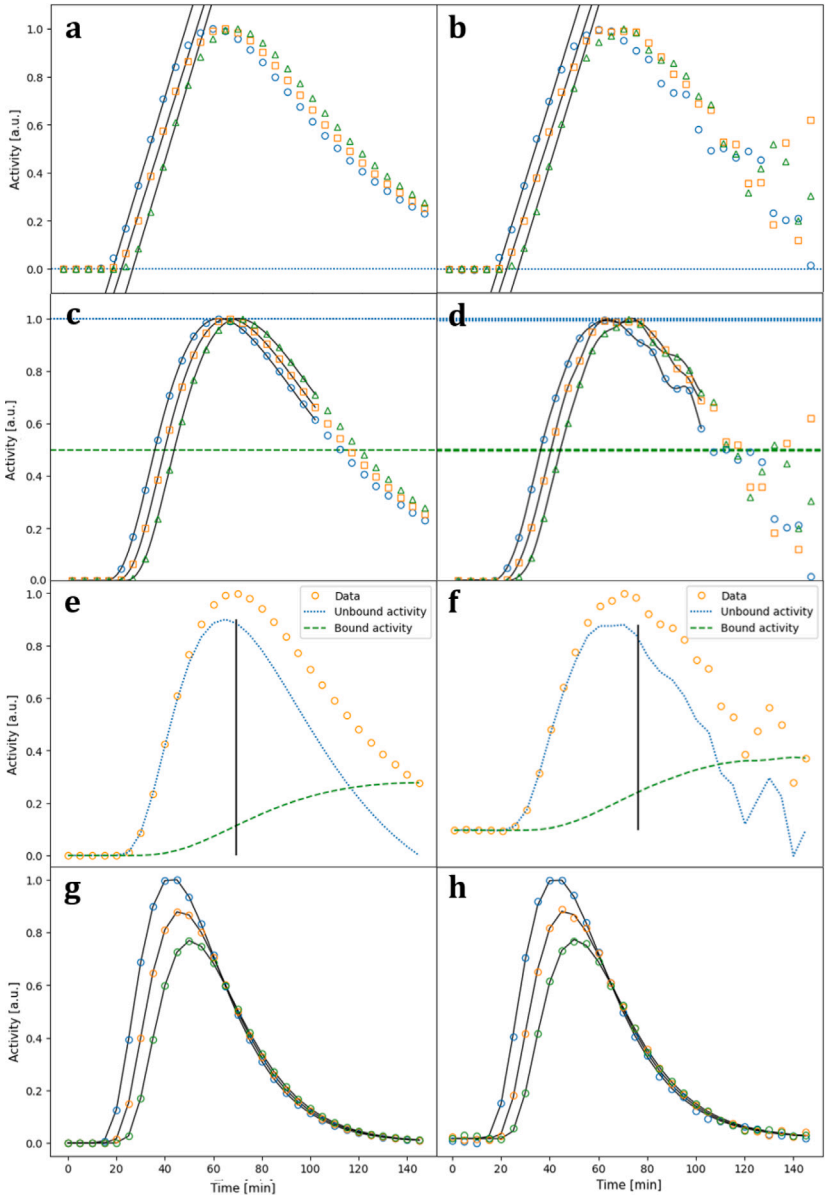

Fig. 8. Application of velocity determination methods on simulated data (see Section 2.3.5) without noise (left) and noisy data (right). Intercept (a)–(b), Half-maximum (c)–(d), McKay (e)–(f), Bühler Model (g)–(h). Reference velocity $v = 5$ mm/min. Derived velocities are noted in Table 1.

algorithm (Fig. 9a). In a second analysis, the points identified by the RANSAC algorithm were shifted either one point in negative or in positive direction (Fig. 9b and c, respectively) along the curve, and the resulting velocities were determined. These shifts emulate small deviations in the determination of the linear part, as they could happen when manually picking the points to include in the regression. In Fig. 9 the red points mark the points used for the respective linear regression.

While the 'standard RANSAC' analysis yielded a velocity of 5.01 ± 7.8% mm/min, thus very close to the ground truth, the velocities determined from the 'offset' analysis resulted in relative differences of 15%–25% with $3.98 \pm 3.8\%$ mm/min for the negative and $5.90 \pm 13.9\%$ mm/min for the positive offset respectively. Each of the three analyses had a high coefficient of determination R^2 in the distance-time fits for velocity estimation (Appendix C).

The high R^2 as well as the visual similarity between the three fits in Fig. 9 show, that a manual identification of the linear part is hardly possible and cannot be done objectively. This user-dependency may result in high errors for the flow velocity when analyzing noisy datasets

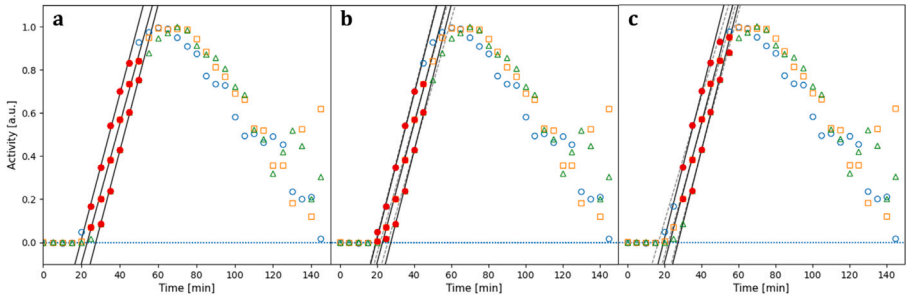

Fig. 9. Velocity determination with the intercept method affected by offsets causing a change in the linear slope for the 'standard' RANSAC analysis (a), a negative offset (b) and a positive offset (c). The black line is the original regression in every figure. Offset regressions are marked by the dashed gray lines. Simulated data (see Section 2.3.5) with a reference velocity of $v = 5$ mm/min.

Table 2
Application of velocity determination methods on simulated data for different types of TACs. Reference velocity 5 mm/min.

			Transport type		
			Uniform	Storage	Exchange
Intercept	Original data	v [mm/min]	4.87 ± 3.9%	5.29 ± 10.02%	2.96 ± 3.38%
	Corrected data	v [mm/min]	5.21 ± 6.3%	4.42 ± 8.6%	2.11 ± 3.8%
Half-maximum	Original data	v [mm/min]	4.95 ± 0.6%	5.04 ± 2.2%	2.07 ± 8.2%
	Corrected data	v [mm/min]	5.13 ± 7.4%	4.12 ± 29%	1.7 ± 9.4%
McKay model	Corrected data	v [mm/min]	−0.76 ± 309%	−3.91 ± 156%	0.27 ± 740%
Bühler model	Original data	v [mm/min]	5.05 ± 1.9%	5.07 ± 2.3%	5.14 ± 9.0%

as well as significant differences in flow speed values depending on how the linear slope is determined.

The RANSAC algorithm can eliminate some of those uncertainties, making the intercept method more robust and better comparable. The accurate velocity determination in the 'standard RANSAC' analysis further supports this finding.

3.1.3. Effect of noise and measurement times on McKay method

The McKay model operates on the assumption that the TAC can be described as the sum of two curves: the moving tracer and the immobilized tracer. Additionally, it assumes that the moving tracer activity is zero at the final value of the TAC (see Section 2.3.3). This leads to two issues: firstly, the method is highly sensitive to noise at later times because it relies on the final TAC value. This is the reason for the failure of the McKay method in Fig. 8f. Secondly, a systematic error in the estimated velocity occurs if the assumption that the moving tracer is zero at the end of the measurement is not met. This explains the high difference between the ground truth and the McKay model estimation for the noiseless dataset since the function value at the last point was still containing a non-zero moving portion.

In experimental data, TACs that end before the moving part equals zero are not unusual as *in vivo* measurements often show very broad pulses (see case study in Section 3.2).

3.1.4. Effect of different transport types on methods

Besides noise, the performance of analysis methods is also subject to the TAC shape, resulting from its underlying transport dynamics. To investigate the suitability of each method for different TAC shapes, their performance was tested with three simulated datasets corresponding to the three transport types presented in Section 2.3.5. Intercept and Half-maximum data were tested for decay-corrected as well as uncorrected original data to evaluate potential differences.

The Intercept method led to high relative standard deviations between 4% and 16% (Table 2). This stems from the method's sensitivity to the choice of the linear part of the curve as discussed in Section 3.1.2. This effect was more prominent in the original data due to the steeper slope in the linear incline. For Uniform transport, the Intercept method retrieved the simulated velocity of 5 mm/min within the error margin given by the standard deviation. The underestimation of the velocity in case of the Storage transport type can be attributed to the difficulty of estimating the linear part on a steady curvature (Fig. C.2 Storage, decay-corrected). Although the distance-time fit for the Exchange transport was decent (Fig. C.6), the Intercept method underestimated the velocity in this type of transport.

In comparison, the Half-maximum method generally yielded results with lower standard deviations in cases where a clear maximum was present in the data, such as the Uniform transport type or non-decay-corrected data, which always exhibit a maximum. The corrected curves of the Storage and Exchange transport do not exhibit a defined maximum but rather run towards a plateau due to ongoing storage (Fig. C.3 Storage/Exchange, decay-corrected). For the analysis of the Storage and Exchange type (decay-corrected) data with the Half-maximum method, the maximum was approximated as the average of the last ten data points, while disregarding strong outliers. This approach weakened the influence of noise, yet the deviation from the true value was still higher than for the Uniform case. In case of the Exchange transport, the Half-maximum method underestimated the true velocity, similar to the Intercept method.

The McKay method relies on the transport dynamics and therefore can only be performed on corrected data. The McKay method yielded far-off results due to its noise sensitivity discussed in Section 3.1.1.

As the decay correction is already integrated into the Bühler model, it is used only with the original, uncorrected data. The Bühler model performs well for all three transport types, with relatively low standard deviation and decent fits characterized by small MSE values of 4.06e−05 for the Uniform, 3.28e−05 for the Storage, and 4.50e−05 for the Exchange transport type.

Neither Half-maximum nor Intercept method can correctly determine the velocity for the Exchange transport type. As described in Section 2.3.5 this specific transport type is characterized by a change of TAC shape between the ROIs, caused by unloading and reloading processes inside the phloem. Distances between TACs can be due to either a time shift relating to the transport velocity or a change of curve shape caused by exchange processes. Both, Intercept and Half-maximum methods are not able to differentiate between these two reasons.

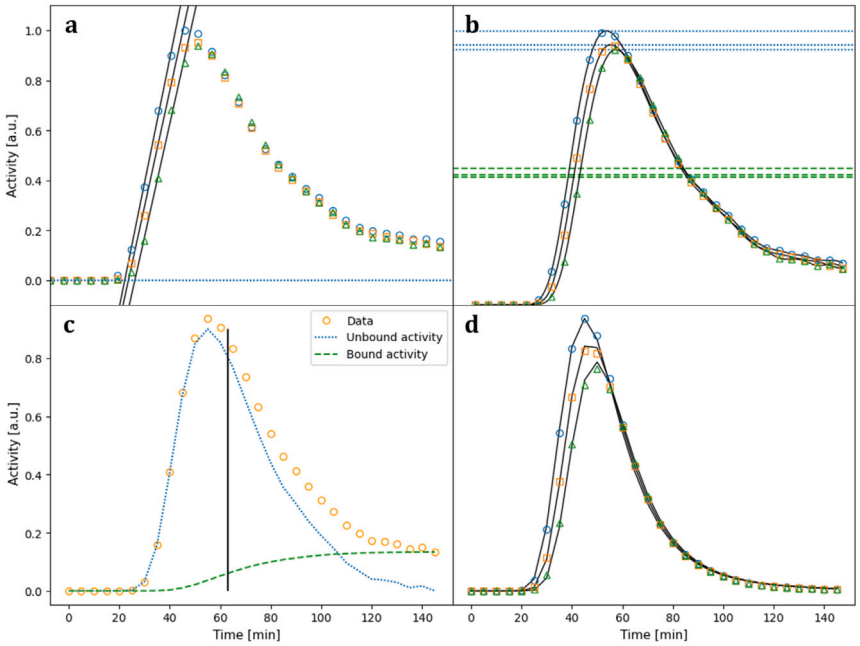

Fig. 10. Application of different methods on TACs measured in the shoot of tomato. Decay-corrected data was used for the Intercept method (a), Half-maximum method (b) and the McKay model (c). The Bühler model (d) operates on uncorrected original data.

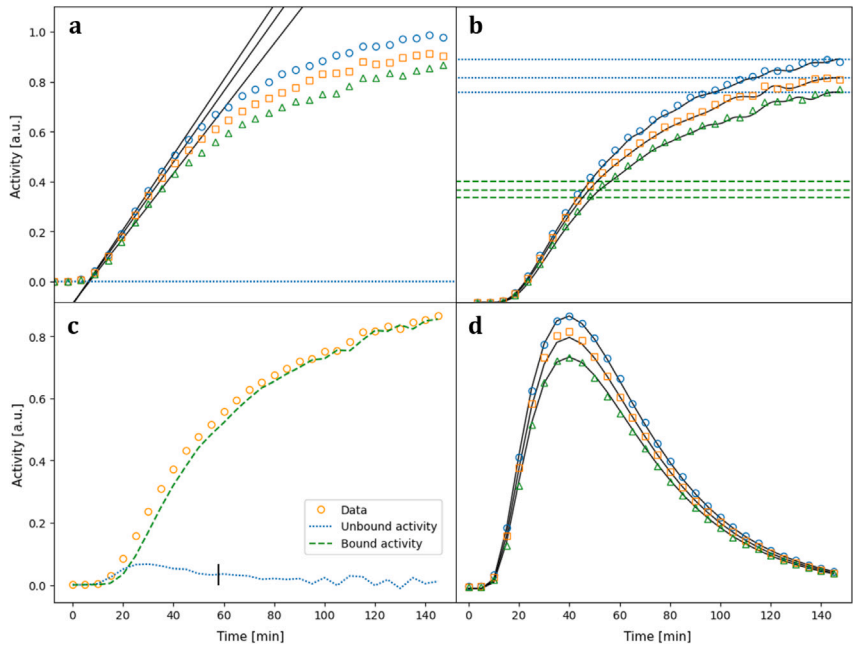

Fig. 11. Application of different methods on TACs measured in the shoot of barley. Decay-corrected data was used for the Intercept method (a), Half-maximum method (b) and the McKay model (c). The Bühler model (d) operates on uncorrected original data.

3.2. Case study - analysis of experimental datasets

To confirm and test the findings based on the simulated datasets, the analysis methods were applied to three experimental test cases, which correspond to the three introduced transport types. To identify shape changes and therefore underlying transport types, the linear correlation between the TACs was tested for each dataset. For each TAC, the average Pearson correlation coefficients against all other TACs were determined. These were 0.93 for tomato, 0.97 for barley and 0.86 for phaseoulus, respectively. A Pearson coefficient greater than 0.9 was considered indicative of a linear relationship, while for a coefficient less than 0.9 we assumed a non-linear relationship. Transport in the stem of a tomato plant (Fig. 10) matched the Uniform transport type, with little storage and no exchange of tracer. In the barley stem (Fig. 11), a large amount of tracer was stored along the transport path, corresponding to the Storage transport type. The transport in a low phaseolus internode (Fig. 12) was characterized by a visible change in TAC shape, thus being an example of the Exchange transport type. In each case, a transport velocity was determined (Table 3) for the decay-corrected data (except for the Bühler model, operating on original data). For the tomato or Uniform transport, all methods worked generally well (Fig. 10) and resulted in similar velocities, except for the McKay method.

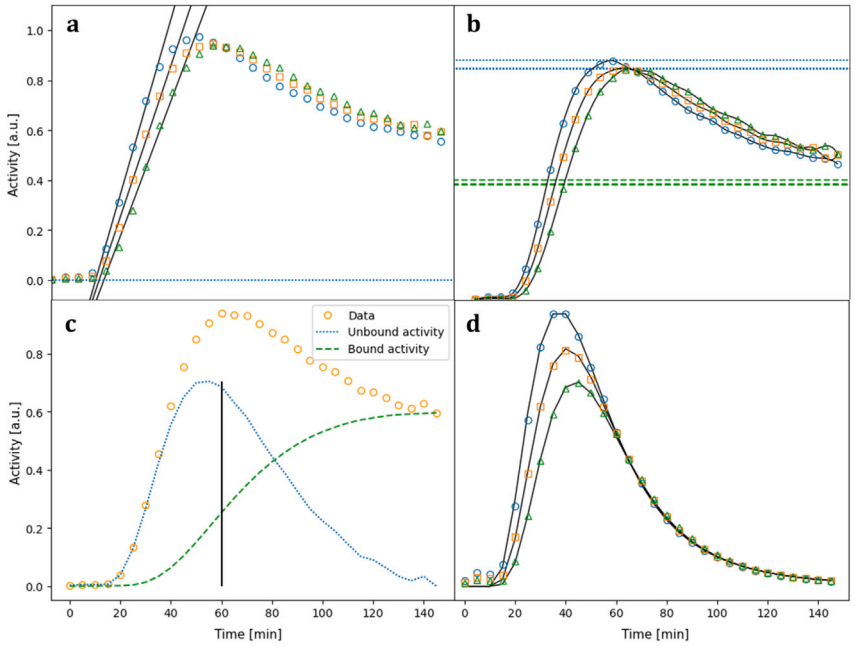

Fig. 12. Application of different methods on TACs measured in the shoot of phaseolus. Decay-corrected data was used for the Intercept method (a), Half-maximum method (b) and the McKay model (c). The Bühler model (d) operates on uncorrected original data.

Table 3
Data analysis with three experimental data sets corresponding to different transport types.

			Method			
			Intercept	Half-Max.	McKay	Bühler
Uniform	Tomato	v [mm/min]	6.4 ± 16.0%	6.3 ± 5.4%	7.5 ± 5.2%	6.3 ± 3.2%
		R^2	0.97	0.99	0.99	–
		MSE	–	–	–	1.19e−04
Storage	Barley	v [mm/min]	30.7 ± 29.7%	7.5[a]±168%	−4.7 ± 107%	35.3 ± 18.9%
		R^2	0.92	0.26[a]	0.47	–
		MSE	–	–	–	5.74e−05
Exchange	Phaseolus	v [mm/min]	5.0 ± 4.6%	3.5 ± 5.7%	4.0 ± 31.7%	7.2 ± 4.1%
		R^2	1	0.99	0.91	–
		MSE	–	–	–	2.20e−04

[a] Barley with Half-maximum method on uncorrected data v = 26.49 ± 5.3%, R^2 = 0.96.

For Barley, the Intercept method as well as the Bühler model yielded velocities in the same order of magnitude, while the Half-maximum and McKay method failed, due to the absence of a maximum and noise in the last data points, respectively (Fig. 11). Using uncorrected data (Fig. C.11), the Half-maximum method yielded a result closer to but still significantly lower than the Intercept method and the Bühler model.

For the phaseolus TACs (Fig. 12) the Intercept and Half-maximum method resulted in excellent distance-time fits, yet the estimated velocities were lower than with the Bühler model. The McKay method resulted in a velocity in between Intercept and Half-Maximum but had a very high standard deviation of over 30%. This difference is to be expected, as the Intercept and Half-maximum method cannot separate between TAC shifts caused by transport or exchange processes as mentioned in 3.1.4. The Bühler method achieved a good fit with a very small MSE and a low relative standard error.

The findings of the case study confirmed the results of simulated data in Section 3.1.4: Intercept, Half-maximum, and the Bühler model performed well for tomato (Uniform transport). The Intercept method generally yielded higher standard deviations, due to slope sensitivity. The McKay method did not work for phaseolus (Exchange) and barley (Storage) and deviated from the other velocities in case of tomato (Uniform). For Uniform and Storage type transport, the Bühler model results were close to either the Half-maximum or the Intercept methods. The transport velocity determined for the phaseolus (Exchange) was different for every method.

4. Conclusion

The evaluation of method performance using both simulated and experimental data highlighted method-specific strengths and weaknesses. Analyzing artificial data with random noise provided clear insights into the noise sensitivity of all methods. However, as the simulated data was both created and analyzed with the Bühler model, it may overestimate its capabilities and is therefore limited for comparing method performance. Therefore, the case study data, reflecting *in vivo* conditions, was far more meaningful for evaluating model performance. Notably, the conclusions from the case study aligned with those from the simulated data, supporting the overall findings. This enabled us to compile a case-specific recommendation on their applicability, as summarized in Fig. 13.

The Half-maximum method is best used in combination with a spline to interpolate the exact time coordinate of maximum and half-maximum. For the Storage type transport, the Half-maximum method

Type	Intercept RANSAC	Half-max. Spline	Half-max. Sigmoidal	McKay model	Bühler model family
	Method				
Uniform	~	✓	X	X	✓
Storage	~	~	~	X	✓
Exchange	X	X	X	X	✓

Fig. 13. Recommendations of utilization of the introduced methods depending on the three characteristic transport types. A green checkmark means unconditional recommendation for that transport type. A yellow tilde means limited recommendation, a red X means no recommendation.

is limited, as a non-clear maximum with high noise levels leads to high uncertainties and errors in velocity determination. In cases where the transport is highly storage-dominated and the maximum represents a noisy plateau, the half-maximum method might yield a more robust result when assuming the maximum to be the average of the point cluster or combined with a sigmoidal fit (logistic regression). Non-decay-corrected data can be analyzed to acquire a rough estimate for the velocity but ultimately should be avoided, as data-driven analysis methods derive information directly from the TAC shape and non-decay-corrected data does not represent transport dynamics.

The Intercept method can prove valuable in cases where the Half-maximum fails, as it is independent of the detectability of the maximum. Still, due to its sensitivity to noise and user subjectivity, the Intercept method is less favorable to use and if necessary should be combined with a rational evaluation of the linear slope such as the RANSAC algorithm.

The McKay method's sensitivity to noise renders it unreliable and therefore impractical to use except maybe for cases with very short tracer pulses and low noise levels.

The compartmental model family yields reliable results in each of the analyzed cases, with model M01 being fit for Uniform and model M02 for Storage type transport while model M13 performs in modeling transport with exchange processes.

When analyzing TACs that change shape in between ROIs due to ongoing exchange processes, each of the introduced methods resulted in a different velocity. As described in Section 3.1.4 this is expected as data-driven methods cannot differentiate between transport and exchange processes, both of which influence the TAC shape. These data-driven methods (here Intercept, Half-maximum, and McKay) assume a linear relationship between the chosen reference time points of each TAC. However, this linear relationship does not hold for the Exchange transport type data. It can be observed that, when analyzing Exchange-type transport compared to the Half-maximum method (which is assumed to be closer to an average velocity), the Intercept method usually yields higher velocities, which can be understood as front velocities. However, since both methods are significantly influenced by the exchange processes, it remains challenging to discern the specific dynamics represented by the calculated velocities.

In general, a quantitative analysis that compares PET data across multiple studies requires a velocity estimation method that is robust regardless of the underlying transport dynamics. The model velocity in the Bühler model fulfills this requirement, as it equals the flow speed only in the transporting compartment while allowing storage and exchange to be modeled with separate exchange parameters.

In conclusion, when applied within their limitations and preferable with additional helping operations such as the RANSAC algorithm or a spline, the Intercept as well as the Half-maximum method have a justification that goes beyond empiric experience. With a prior thorough analysis of the data, the TACs, and the underlying transport dynamics, it is possible to pick a method that will yield an accurate velocity. Although the Bühler model in theory covers all the functionalities of the Intercept and Half-maximum method, it is still recommended to use it in combination with at least one of these methods. This either confirms model results or provides further information on the transport dynamics should the resulting velocities between model and data-driven approaches differ. Furthermore, in comparison to the data-driven approaches, the Bühler model provides the possibility to not only obtain a comparable velocity in cases where TAC dynamics are characterized by exchange but also estimates storage and exchange rates. This is why it is highly recommended to utilize the Bühler model when analyzing tracer transport experiments, especially when the underlying transport dynamics are unclear.

CRediT authorship contribution statement

Hannah Lanzrath: Writing – review & editing, Writing – original draft, Visualization, Software, Methodology, Investigation, Formal analysis, Conceptualization. **Eric von Lieres:** Writing – review & editing, Supervision, Methodology, Conceptualization. **Ralf Metzner:** Writing – review & editing, Resources, Investigation. **Gregor Huber:** Writing – review & editing, Supervision, Methodology, Formal analysis, Conceptualization.

Declaration of competing interest

The authors declare that they have no known competing financial interests or personal relationships that could have appeared to influence the work reported in this paper.

Acknowledgments

The authors gratefully acknowledge Samuel Leweke, Johannes Schmölder, Jan Breuer, Ronald Jäpel, Jayghosh Rao and Jazib Hassan for their help in implementing the Bühler model as the MCT model within the CADET framework. Furthermore, we thank Mascha Schmidt for her work on the MeVisLab TAC-ROI tool as well as Esther Breuer, Marco Dautzenberg and Antonia Chlubek for their technical support during data collection.

Appendix A. Plant growing and experimental conditions

In the case study, the tracer transport dynamics in the stem of three different plant species tomato, barley, and phaseolus were investigated, using a custom-built vertical-bore PET system known as PhenoPET. It features a field of view with a diameter of 180 mm and a height of 200 mm. [20,21].

Tomato (*Solanum lycopersicum*, cv. Moneymaker): The plant was cultivated in a greenhouse, with a daytime temperature of 20 ± 1 °C, a nighttime temperature of 16 ± 1 °C, and humidity maintained at 55 ± 5%. Supplemental light was provided for 14 h each day using SON-T Agro 400 W Philips metal halogen vapor lamps. During the time span of the measurements, the temperature in the climate chamber housing the PET was set at 20 ± 1 °C during the day and 16 ± 1 °C at night (16 h/8 h). Humidity was maintained at 60 ± 2%, and light

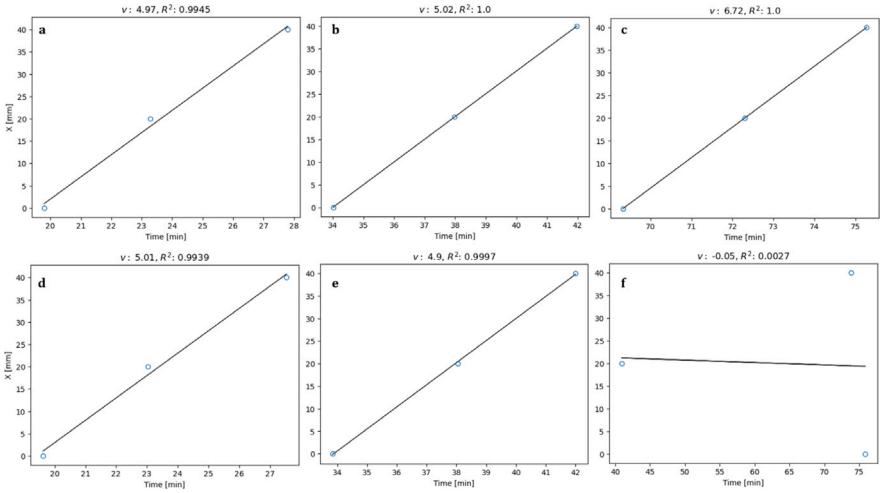

Fig. C.1. Distance-time fits of noiseless (upper) data and noisy (lower) data relating to Fig. 8 and Table 1, Intercept (a)+(d), Half-maximum (b)+(e), McKay (c)+(f). v is the derived velocity and R^2 relates to the fit quality.

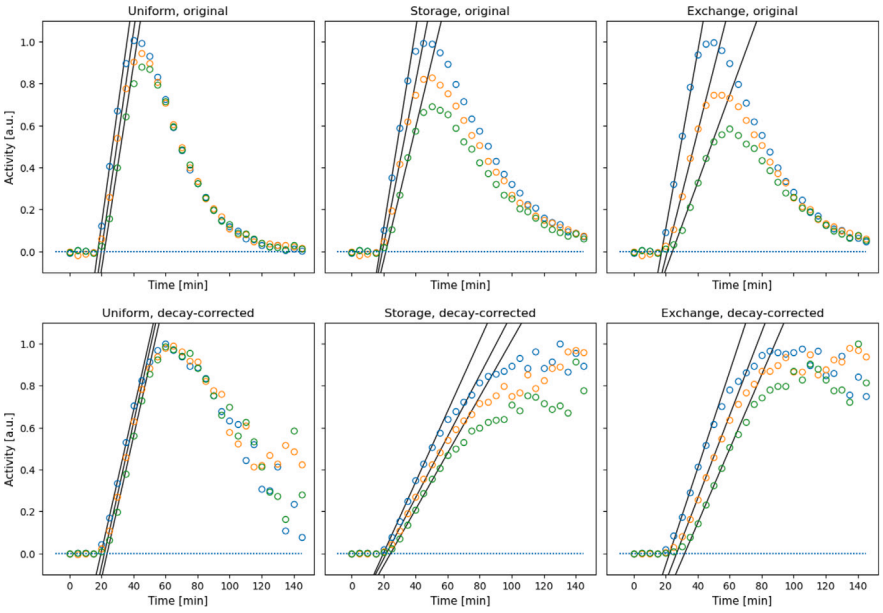

Fig. C.2. Intercept method applied to simulated data (see Section 2.3.5) of the three different transport types corresponding to Table 2. Original data in the upper row, and decay-corrected data in the lower row. For color coding of figure elements refer to Fig. 3.

Table B.4
Parameters of all simulations used to create artificial data in this study. A stretched Gauss boundary condition was used according to Eq. (6). For exchange rates e_{ij} and models see Figs. 4 and 6, respectively.

Figure/Table	v [mm/min]	p_2 [min]	p_3	p_4	p_1	Model	e_{12}	e_{21}	e_{23}	Noise
Fig. 2	5	30	8	3	1	M01	–	–	–	–
Fig. 3(a)–(d)+(f)	5	30	8	3	1	M01	–	–	–	–
Fig. 3(e)	5	30	8	3	1	M02	0.06	–	–	–
Fig. 4(b)	5	20	8	2	1	M13	0.01	0.008	0.005	–
Fig. 7(a)	5	30	8	3	1	M01	–	–	–	–
Fig. 7(b)	5	30	8	3	1	M02	0.06	–	–	–
Fig. 7(c)	5	30	8	3	1	M13	0.5	0.2	0.01	–
Table 1 noiseless/Fig. 8l.	5	40	10	2	1	M01	–	–	–	–
Table 1 noisy/Fig. 8r.	5	40	10	2	1	M01	–	–	–	0.7%
Fig. 9	5	40	10	2	1	M01	–	–	–	0.7%
Table 2 Uni./Figs. 10–13	5	40	10	2	1	M01	–	–	–	0.7%
Table 2 Stor./Figs. 10–13	5	40	10	2	1	M02	0.06	–	–	0.7%
Table 2 Exch./Figs. 10–13	5	40	10	2	1	M13	0.5	0.2	0.01	0.7%

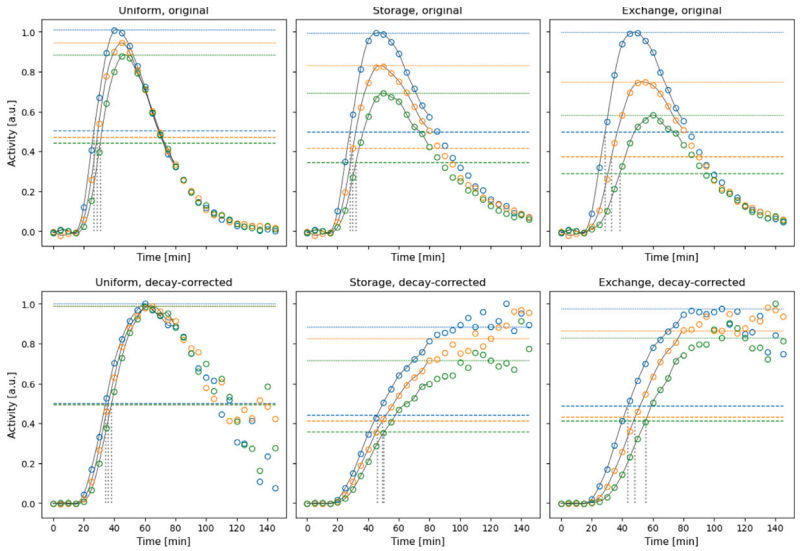

Fig. C.3. Half-Maximum method applied to simulated data (see Section 2.3.5) of the three different transport types corresponding to Table 2. Original data in the upper row, and decay-corrected data in the lower row. The circles are the datapoints and dashed lines mark the maximum as well as half-maximum of the respective ROIs.

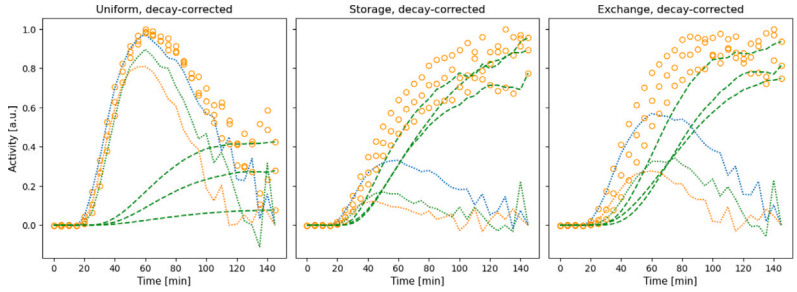

Fig. C.4. McKay method applied to simulated data (see Section 2.3.5) of the three different transport types corresponding to Table 2. Only for decay-corrected data. For color coding of figure elements refer to Fig. 3.

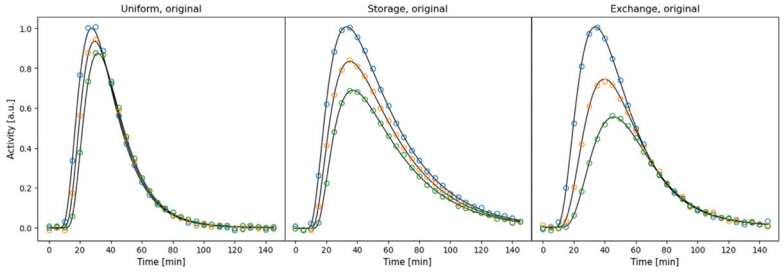

Fig. C.5. Bühler model fits applied to simulated data (see Section 2.3.5) of the three different transport types Uniform (MSE 4.06e−05), Storage (MSE 3.28e−05) and Exchange (MSE 4.50e−05) corresponding to Table 2. Only for non-decay-corrected original data. For color coding of figure elements refer to Fig. 3.

was provided by in-house built LED lamps with a PAR intensity of 300 µmol/m^2 s. The cuvette received conditioned gas from a gas mixing unit with temperature 19 ± 1 °C, humidity 80 ± 1% and CO_2 380 ± 5 ppm controlled.

Barley (*Hordeum vulgare*, cv. Barke): The plant was grown in a climate chamber, maintaining a temperature of 20 ± 1 °C during the day and 16 ± 1 °C at night (16 h/8 h). Humidity was set at 60 ± 1% and lighting alternated between five 400 W HPI and five 400 W SON-T lamps. On the day of measurement, the temperature in the PET climate chamber was set to 22 ± 1 °C during the day and 16 ± 1 °C at night (16 h/8 h), with humidity at 60 ± 2%. Lighting conditions were consistent with those described for Tomato. The cuvette received conditioned gas with temperature 23 ± 1 °C, humidity 62 ± 1%, and CO_2 400 ± 5ppm controlled.

Phaseolus (*Phaseolus vulgaris*, cv. Shiny Fardenlosa): The plant was grown in a climate chamber, with a temperature of 20 ± 1 °C during the day and 18 ± 1 °C at night (16 h/8 h). Humidity was maintained at 60 ± 2%, and lighting alternated between five 400WHPI and five 400 W SON-T lamps. On the day of measurement, the temperature in the PET climate chamber was set to 22 ± 1 °C during the day and 16 ± 1 °C at night (16 h/8 h), with humidity at 60 ± 3%. Lighting conditions were consistent with those described for Tomato. Tracer production followed the same procedure as for Tomato and Barley. The cuvette received

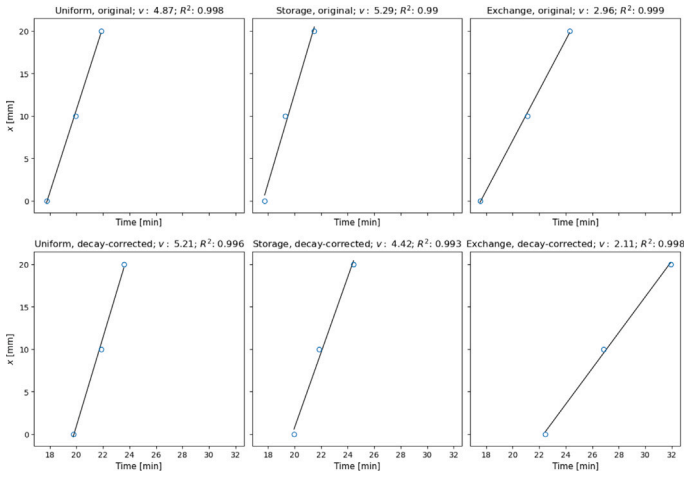

Fig. C.6. Distance-time fits of the Intercept method for different transport types, relating to Fig. C.2, Table 2. v is the derived velocity and R^2 relates to the fit quality.

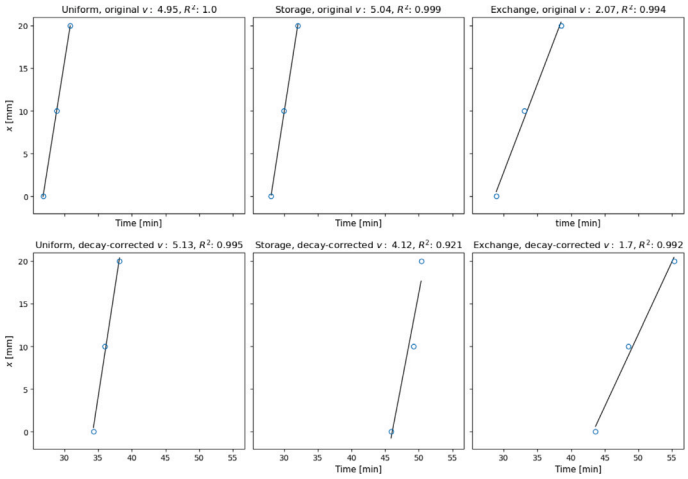

Fig. C.7. Distance-time fits of the Half-maximum method for different transport types, relating to Fig. C.3, Table 2. v is the derived velocity and R^2 relates to the fit quality.

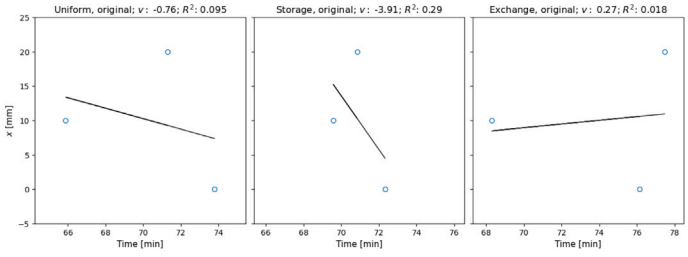

Fig. C.8. Distance-time fits of the McKay for different transport types, relating to Fig. C.4, Table 2. v is the derived velocity and R^2 relates to the fit quality.

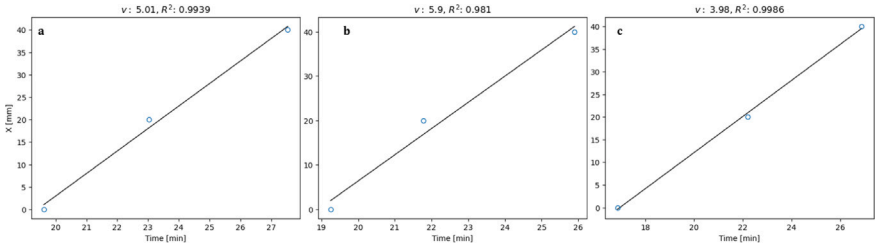

Fig. C.9. Distance-time fits for the analysis of change in the linear TAC part used for the Intercept method for the 'standard' RANSAC analysis (a), a negative offset (b) and a positive offset (c). See Fig. 9. v is the derived velocity and R^2 relates to the fit quality.

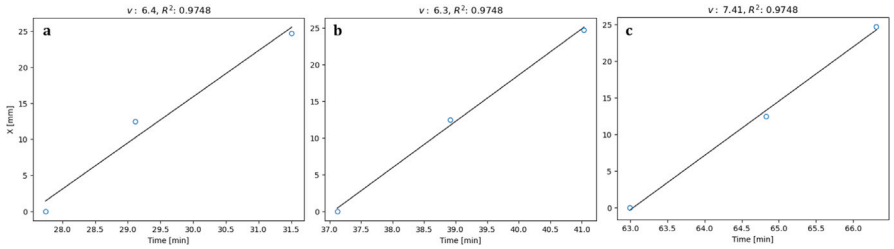

Fig. C.10. Distance-time fits for different methods on TACs measured in the shoot of tomato. Analysis was performed with the Intercept method (a), the Half-maximum method (b) and the McKay model (c).v is the derived velocity and R^2 relates to the fit quality.

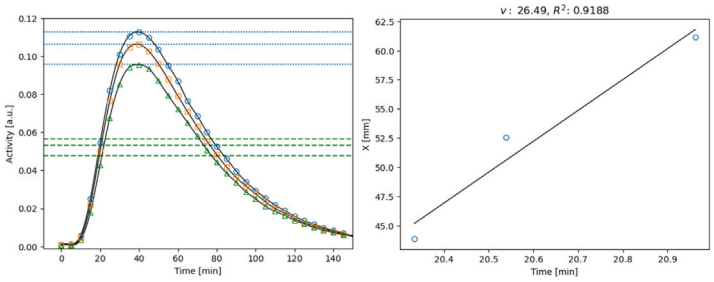

Fig. C.11. Alternative maximum fit and distance-time fit for the maximum method on TACs measured in the shoot of barley. v is the derived velocity and R^2 relates to the fit quality.

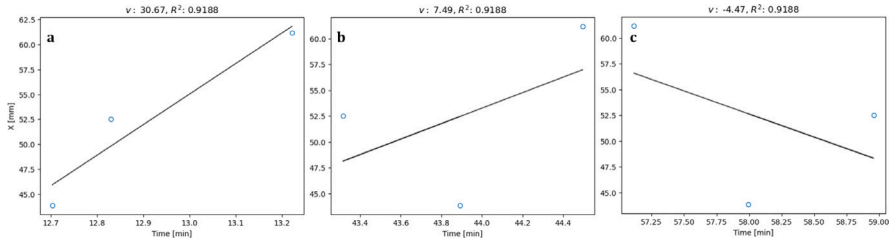

Fig. C.12. Distance-time fits for methods on TACs measured in the shoot of barley. Analysis was performed with the intercept method (a), the half-maximum method (b) and the McKay model (c). v is the derived velocity and R^2 relates to the fit quality.

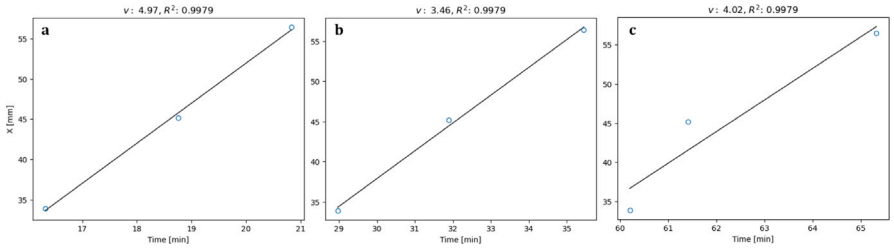

Fig. C.13. Distance-time fits for methods on TACs measured in the shoot of Phaseolus. Analysis was performed with the intercept method (a), the half-maximum method (b) and the McKay model (c). v is the derived velocity and R^2 relates to the fit quality.

conditioned gas with temperature 24 ± 1 °C, humidity $68 \pm 3\%$, and CO_2 400 ± 5 ppm controlled.

Appendix B

B.1. Artificial data parameter specifications

Table B.4 references all artificially created data used in this study. The simulations were performed with the Multichannel transport model of the CADET framework.

Appendix C. Additional figures

C.1. Noise experiment

See Fig. C.1.

C.2. Transport types

See Figs. C.2–C.9.

C.3. Case study

See Figs. C.10–C.13.

Data availability

Data will be made available on request.

References

[1] N. Michele Holbrook, Maciej A. Zwieniecki, Vascular Transport in Plants, Academic Press, 2005, http://dx.doi.org/10.1016/B978-0-12-088457-5.X5000-X.

[2] André Lacointe, Peter E.H. Minchin, Modelling phloem and xylem transport within a complex architecture, Funct. Plant Biol. (ISSN: 14454408) (2008) http://dx.doi.org/10.1071/FP08085.

[3] Veerle De Schepper, Kathy Steppe, Development and verification of a water and sugar transport model using measured stem diameter variations, J. Exp. Bot. (ISSN: 00220957) 61 (8) (2010) http://dx.doi.org/10.1093/jxb/erq018.

[4] Henrik Hartmann, Michael Bahn, Mariah Carbone, Andrew D. Richardson, Plant carbon allocation in a changing world – challenges and progress: introduction to a virtual issue on carbon allocation, New Phytol. 227 (4) (2020) 981–988, http://dx.doi.org/10.1111/nph.16757.

[5] S. Jahnke, Ulrike Schlesinger, G.B. Feige, E.J. Knust, Transport of photoassimilates in young trees of fraxinus and sorbus: Measurement of translocation in vivo, Bot. Acta (ISSN: 09328629) 111 (1998) http://dx.doi.org/10.1111/j.1438-8677.1998.tb00714.x.

[6] Siegfried Jahnke, Marion I. Menzel, Dagmar Van Dusschoten, Gerhard W. Roeb, Jonas Bühler, Senay Minwuyelet, Peter Blümler, Vicky M. Temperton, Thomas Hombach, Matthias Streun, Simone Beer, Maryam Khodaverdi, Karl Ziemons, Heinz H. Coenen, Ulrich Schurr, Combined MRI-pet dissects dynamic changes in plant structures and functions, Plant J. (ISSN: 09607412) 59 (2009) http://dx.doi.org/10.1111/j.1365-313X.2009.03888.x.

[7] Jonas Bühler, Eric von Lieres, Gregor Huber, A class of compartmental models for long-distance tracer transport in plants, J. Theoret. Biol. (ISSN: 00225193) (2014) http://dx.doi.org/10.1016/j.jtbi.2013.09.023.

[8] Michiel Hubeau, Kathy Steppe, Plant-PET scans: In vivo mapping of xylem and phloem functioning, Trends Plant Sci. (ISSN: 13601385) 20 (2015) 676–685, http://dx.doi.org/10.1016/j.tplants.2015.07.008.

[9] Johannes Liesche, Phloem methods and protocols, in: Springer Protocols, Springer Science+Business Media, LLC, 2019.

[10] Michael Thorpe, Peter Minchin, In vivo veritas: Radiotracers in studies of phloem transport of carbohydrate, in: Methods in Molecular Biology (Clifton, N.J.), vol. 2014, Springer Nature, ISBN: 978-1-4939-9561-5, 2019, pp. 177–194, http://dx.doi.org/10.1007/978-1-4939-9562-2_15.

[11] M.T. Tyree, Horwitz-type models of tracer distribution during unidirectional translocation, in: Phloem Transport, Springer, 1975, http://dx.doi.org/10.1007/978-1-4684-8658-2_15.

[12] A.J.E. Van Bel, The phloem, a miracle of ingenuity, Plant Cell Environ. (ISSN: 01407791) 26 (2003) http://dx.doi.org/10.1046/j.1365-3040.2003.00963.x.

[13] E.J. Williams, J.E. Dale, J. Moorby, J. Scobie, Variation in translocation during the photoperiod: Experiments feeding 11co2 to sunflower, J. Exp. Bot. (ISSN: 00220957) (1979) http://dx.doi.org/10.1093/jxb/30.4.727.

[14] Peter E.H. Minchin, Michael R. Thorpe, Using the short-lived isotope 11C in mechanistic studies of photosynthate transport, (ISSN: 14454408) 2003, http://dx.doi.org/10.1071/FP03008.

[15] Benjamin A. Babst, Richard A. Ferrieri, Dennis W. Gray, Manuel Lerdau, David J. Schlyer, Michael Schueller, Michael R. Thorpe, Colin M. Orians, Jasmonic acid induces rapid changes in carbon transport and partitioning in populus, New Phytol. (ISSN: 0028646X) (2005) http://dx.doi.org/10.1111/j.1469-8137.2005.01388.x.

[16] Ryuichi Suwa, Shu Fujimaki, Nobuo Suzui, Naoki Kawachi, Satomi Ishii, Koichi Sakamoto, Nguyen Tran Nguyen, Hirofumi Saneoka, Pravat K. Mohapatra, Reda E. Moghaieb, Shinpei Matsuhashi, Kounosuke Fujita, Use of positron-emitting tracer imaging system for measuring the effect of salinity on temporal and spatial distribution of 11c tracer and coupling between source and sink organs, Plant Sci. (ISSN: 01689452) 175 (2008) 210–216, http://dx.doi.org/10.1016/j.plantsci.2008.03.022.

[17] Christopher Vincent, Peter E.H. Minchin, Johannes Liesche, Noninvasive determination of phloem transport speed with carbon-14 (14C), in: Johannes Liesche (Ed.), Phloem: Methods and Protocols, Springer New York, New York, NY, ISBN: 978-1-4939-9562-2, 2019, pp. 153–162, http://dx.doi.org/10.1007/978-1-4939-9562-2_13.

[18] R.M.L. McKay, G.R. Palmer, X.P. Ma, D.B. Layzell, B.T.A. McKee, The use of positron emission tomography for studies of long-distance transport in plants: uptake and transport of 18F, in: Plant, Cell 'I&' Environment, 1988, http://dx.doi.org/10.1111/j.1365-3040.1988.tb01911.x.

[19] Michiel Hubeau, Jens Mincke, Christian Vanhove, Jan Courtyn, Stefaan Vandenberghe, Kathy Steppe, Plant-PET to investigate phloem vulnerability to drought in populus tremula under changing climate regimes, Tree Physiol. (ISSN: 17584469) 39 (2018) http://dx.doi.org/10.1093/treephys/tpy131.

[20] Ralf Metzner, Antonia Chlubek, Jonas Bühler, Daniel Pflugfelder, Ulrich Schurr, Gregor Huber, Robert Koller, Siegfried Jahnke, In vivo imaging and quantification of carbon tracer dynamics in nodulated root systems of pea plants, Plants (ISSN: 22237747) 11 (2022) http://dx.doi.org/10.3390/plants11050632.

[21] Carsten Hinz, Siegfried Jahnke, Ralf Metzner, Daniel Pflugfelder, Jürgen Scheins, Matthias Streun, Robert Koller, Setup and characterisation according to NEMA NU 4 of the phenoPET scanner, a PET system dedicated for plant sciences, Phys. Med. Biol. 69 (5) (2024) 055019, http://dx.doi.org/10.1088/1361-6560/ad22a2.

[22] Mascha Schmidt, Jonas Bühler, Daniel Habbel, Ralf Metzner, FZJ TAC-ROI-TOOL, 2024, http://dx.doi.org/10.5281/zenodo.12664701.

[23] Jonas Bühler, Eric von Lieres, Gregor J. Huber, Model-based design of long-distance tracer transport experiments in plants, Front. Plant Sci. (ISSN: 1664462X) (2018) http://dx.doi.org/10.3389/fpls.2018.00773.

[24] Alexander K. Converse, Elizabeth O. Ahlers, Tom W. Bryan, Jackson D. Hetue, Katherine A. Lake, Paul A. Ellison, Jonathan W. Engle, Todd E. Barnhart, Robert J. Nickles, Paul H. Williams, Onofre T. DeJesus, Mathematical modeling of positron emission tomography (PET) data to assess radiofluoride transport in living plants following petiolar administration, Plant Methods (ISSN: 17464811) 11 (2015) http://dx.doi.org/10.1186/s13007-015-0061-y.

[25] Leonard Horwitz, Some simplified mathematical treatments of translocation in plants, Plant Physiol. 33 (2) (1958) 81–93, http://dx.doi.org/10.1104/pp.33.2.81.

[26] Jonas Bühler, Gregor Huber, Friederike Schmid, Peter Blümler, Analytical model for long-distance tracer-transport in plants, J. Theoret. Biol. (ISSN: 00225193) (2011) http://dx.doi.org/10.1016/j.jtbi.2010.11.005.

[27] Samuel Leweke, Eric von Lieres, Chromatography analysis and design toolkit (CADET), Comput. Chem. Eng. (ISSN: 0098-1354) 113 (2018) 274–294, http://dx.doi.org/10.1016/j.compchemeng.2018.02.025.

[28] Samuel Leweke, Unified Modeling and Efficient Simulation of Chromatographic Separation Processes (Ph.D. thesis), Rheinisch-Westfälische Technische Hochschule Aachen, Aachen, 2021, http://dx.doi.org/10.18154/RWTH-2022-01184.

[29] Samuel Leweke, Johannes Schmölder, Eric von Lieres, Jayghosh Rao, Jazib Hassan, William Heymann, Jan Breuer, Jonathan Rocher, Salah Azzouzi, modsim/CADET: Version 4.4.0, 2023, http://dx.doi.org/10.5281/zenodo.8179015.

[30] Jonas Bühler, Gregor Huber, Eric von Lieres, Finite volume schemes for the numerical simulation of tracer transport in plants, Math. Biosci. (ISSN: 18793134) (2017) http://dx.doi.org/10.1016/j.mbs.2017.02.009.

[31] Martin A. Fischler, Robert C. Bolles, Random sample consensus: a paradigm for model fitting with applications to image analysis and automated cartography, Commun. ACM (ISSN: 0001-0782) 24 (6) (1981) 381–395, http://dx.doi.org/10.1145/358669.358692.